ACS Catalysis

Research Article

pubs.acs.org/acscatalysis

Engineering Complex, Layered Metal Oxides: High-Performance Nickelate Oxide Nanostructures for Oxygen Exchange and Reduction

Xianfeng Ma,[†,⊥] Juliana S. A. Carneiro,[†,⊥] Xiang-Kui Gu,[†,⊥] Hao Qin,[†] Hongliang Xin,[‡] Kai Sun,[§] and Eranda Nikolla*[,†]

[†]Department of Chemical Engineering and Materials Science, Wayne State University, Detroit, Michigan 48202, United States

[‡]Department of Chemical Engineering, Virginia Polytechnic Institute and State University, Blacksburg, Virginia 24061, United States

[§]Department of Materials Science and Engineering, University of Michigan, Ann Arbor, Michigan 48109, United States

Supporting Information

ABSTRACT: Synthetically tuning the surface properties of many oxide catalysts to optimize their catalytic activity has been appreciably challenging, given their complex crystal structure. Nickelate oxides (e.g., $La_2NiO_{4+\delta}$) are among complex, layered oxides with great potential toward efficiently catalyzing chemical/electrochemical reactions involving oxygen (oxygen reduction, ammonia oxidation). Our theoretical calculations show that the surface structure of $La_2NiO_{4+\delta}$ plays a critical role in its activity, with the (001)-Ni oxide-terminated surface being the most active. This is demonstrated through the effect on the energetics associated with surface oxygen exchange, a key process in reactions involving oxygen on these oxides. Using a reverse microemulsion method, we have synthesized $La_2NiO_{4+\delta}$ nanorod-structured catalysts highly populated by (001)-Ni oxide-terminated surfaces. We show that these nanostructures exhibit superior catalytic activity toward oxygen exchange/reduction as compared with traditional catalysts while maintaining stability under reaction conditions. The findings reported here pave the way for engineering complex metal oxides with optimal activity.

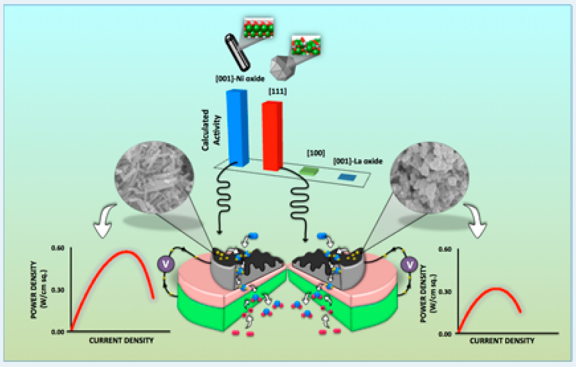

KEYWORDS: *nickelate oxide, solid oxide fuel cell, density functional calculations, oxygen exchange, catalysis*

INTRODUCTION

The surface structure of heterogeneous catalysts and electrocatalysts plays a critical role in determining their activity and selectivity.[1] With recent advancements in solution-based synthesis approaches and the predictive power of theoretical calculations, the surface structure of metals and simple metal oxides can be tuned to obtain unparalleled catalytic performance for many relevant reactions.[2] Nevertheless, control over the surface reactivity of complex, layered metal oxide-based catalysts (e.g., nickelate oxides) is still appreciably challenging. Identifying ways to tap into understanding and optimizing the physicochemical properties of complex metal oxides can significantly expand the window of technically relevant catalytic materials.

Nickelate oxides (e.g., $La_2NiO_{4+\delta}$, LNO) are among complex, layered oxides with great potential toward efficiently catalyzing chemical and electrochemical reactions involving oxygen (e.g., oxygen evolution/reduction and ammonia oxidation).[3] They are mixed ionic and electronic conducting materials that belong to the Ruddlesden−Popper series, composed of alternating rocksalt-like and perovskite-like layers (Figure 1a). They are characterized by their hyper-stoichiometry of oxygen in the lattice that is accommodated via the rocksalt-like layers.[3d,4] It has been shown that oxygen chemistry on nickelate oxides is governed by their ability to catalyze the surface oxygen exchange process.[5] This process involves the catalytic exchange of gas-phase oxygen with oxygen ions in the lattice of an ion-conducting oxide. Although the oxygen transport mechanisms of nickelate oxides have been well investigated,[6] limited understanding of the factors that govern the surface oxygen exchange process in these materials exists. A recent report from Burriel et al. shows that in the case of Sr-doped $La_2NiO_{4+\delta}$, the La oxide-terminated surface governs the surface oxygen chemistry on these materials.[5b] On the other hand, a report from Read et al. suggests that the Ni^{3+} atoms in the outmost layer are responsible for the catalytic activity of nickelate oxides.[3d] Furthermore, for the most part, nickelate oxides have been synthesized mainly using thermochemical and thin film synthesis approaches, which lead to low-surface-area structures with limited appeal for catalytic applications.[4,6a,b]

In this work, we demonstrate, through a combination of quantum chemical density functional theory (DFT) calculations, controlled synthesis of well-defined nanostructures, state-of-the-art characterization techniques (atomic level imaging and electron energy loss spectroscopy), and isotopic

Received: April 10, 2015
Published: May 22, 2015

DOI: 10.1021/acscatal.5b00756
ACS Catal. 2015, 5, 4013−4019

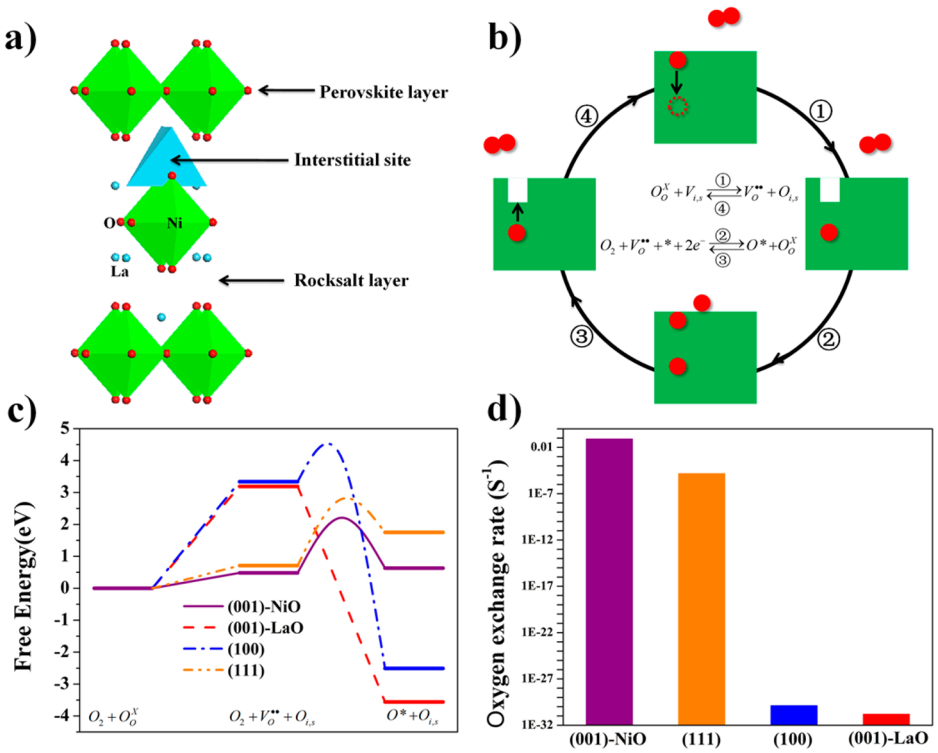

Figure 1. (a) The structure of LNO and the position of the oxygen interstitial site. (b) The mechanism for oxygen exchange on LNO along with the Kröger–Vink notation of the elementary steps, where O_O^X is lattice O on the surface layer, $V_{i,s}$ is a vacant interstitial site in the bulk, $O_{i,s}$ is an interstitial oxygen atom, $V_O^{\bullet\bullet}$ is an oxygen vacancy site on the surface layer, O_2 represents gas-phase oxygen, and O* is an adsorbed oxygen adatom. (c) Free energy surface of the oxygen exchange process (shown in b) on (001), (100), and (111) LNO surfaces. (d) Calculated surface oxygen exchange rates for LNO surfaces at 773 K and 0.21 atm O_2 pressure.

labeling kinetic studies, that engineering the surface of nickelate oxides (i.e., $La_2NiO_{4+\delta}$, LNO) can significantly enhance their catalytic activity toward surface oxygen exchange. DFT calculations show that (001)-Ni oxide-terminated LNO surfaces exhibit the highest rates for oxygen exchange by providing the best compromise between the energetics associated with oxygen adsorption/desorption and surface oxygen vacancy formation.

LNO nanorods, predominantly terminated by (001)-Ni oxide surface facets, were synthesized using a well-controlled reverse microemulsion synthesis method and characterized using atomic-resolution high angle annular dark field (HAADF) imaging along with electron energy-loss spectroscopy (EELS) performed using an aberration-corrected scanning transmission electron microscope (STEM). Our isotope-labeled thermochemical kinetic studies showed that the activation barrier for thermochemical oxygen exchange is significantly lower on the LNO nanorods as compared with the traditional polyhedron-type LNO catalyst. Electrochemical studies using symmetric cells demonstrated that the area-specific resistances associated with the electrochemical oxygen exchange were significantly lower on electrodes containing LNO nanorods than the ones with LNO spheres. Incorporation of the LNO nanorods as cathode electrocatalysts in SOFCs led to a significant increase in the electrochemical rates for oxygen reduction (current densities) as compared with SOFCs containing traditional LNO catalyst or state-of-the-art lanthanum strontium manganite (LSM) catalyst. We also found that the LNO nanorods exhibited high stability under electrochemical conditions. The findings reported in this work lay the groundwork for enhancing the catalytic activity of complex metal oxide catalysts via engineering of their surface structure.

THEORETICAL AND EXPERIMENTAL SECTION

Density Functional Theory Calculations. DFT calculations were performed using the Vienna ab initio Simulation Package (VASP),[7] and Perdew–Burke–Ernzerhof (PBE) exchange-correlation functional.[8] The Kohn–Sham equations were solved by a plane-wave basis set with a kinetic energy cutoff of 400 eV. The optimized lattice constants of bulk La_2NiO_4, with tetragonal $I4/mmm$ structure, are a = 3.86 Å and c = 12.44 Å, which agrees well with experimental values and previous calculations.[9] To model La_2NiO_4 (001), (100), and (111) surfaces, the 13-layer slab model was used with a (2 × 2) unit cell (Figure S1, Supporting Information). A (2 × 2 × 1) k-point mesh was used to sample the surface Brillouin zone, and a 12 Å vacuum was introduced with correction of the dipole moment between the repeated slabs along the z direction. During optimization, the bottom four layers of the slab were fixed, while the remaining atoms were relaxed until the residual force was <0.02 eV/Å. DFT+U[10] was used for Ni 3d orbitals with a value of $U - J$ = 6.4 eV.[11] We note that the defected $La_2NiO_{4+\delta}$ (δ = 0.125) was also investigated. We found that the influence of bulk interstitial O on surface oxygen vacancy formation energy was only 0.02 eV, compared with that on stoichiometric La_2NiO_4. Thus, we used the stoichiometric La_2NiO_4 for DFT calculations in the present work. The barriers were calculated by the CI-NEB method.[12] The details of the microkinetic modeling analysis can be found in the Supporting Information.

DOI: 10.1021/acscatal.5b00756
ACS Catal. 2015, 5, 4013–4019

Catalyst Synthesis and Characterization. The nanostructured LNO catalysts were prepared using the reverse-microemulsion-assisted sol−gel method as reported previously.[13] Details are found in the Supporting Information. Atomic resolution HAADF imaging and EELS spectrum imaging were performed in STEM mode on a double-aberration-corrected JEOL JEM-3100R05 microscope equipped with a cold field-emission electron source and a Gatan 965 energy filter system. All operations were conducted at an accelerating voltage of 300 kV with a probe forming semiangle of roughly 22 mrad and collection of semiangles around 50 and 40 mrads for HAADF imaging and EELS, respectively. The STEM-EELS spectrum imaging data sets were collected at 0.3 s/spectrum and a 0.15 nm/step. The obtained data were processed by multiple linear least-squares (MLLS) fitting for the spectrum data set using Gatan Digital Micrograph software to resolve overlapping edges in the EELS spectra using standard EELS spectra taken from commercial La_2O_3 and Ni oxide samples under the same experimental conditions.[14]

Oxygen Isotopic Exchange Kinetic Studies. All experiments were conducted in a continuous flow system consisting of three gas lines connected to a reactor and a mass spectrometer (QP 2010 Ultra, Shimadzu). In each experiment, an appropriate amount of sample (~0.020 g) was loaded into the reactor and heated to 923 K under flowing Ar to remove any impurities in the sample. This was followed by changing the temperature to the desired value and switching the gas to the oxygen isotope $^{16}O_2$ (2% mole of $^{16}O_2$, 2% mole of Ar, balanced by He). When the steady state was reached, the feed gas was switched to oxygen isotope $^{18}O_2$ (2% mole of $^{18}O_2$, balanced by He) using the same flow rate, and the reaction was allowed to proceed. The transient changes in the isotopic composition ($^{16}O_2$, $^{18}O_2$, $^{16}O^{18}O$) were continuously monitored by mass spectrometry. The reaction temperature was varied from 723 to 923 K. Turnover frequencies (TOF) were defined as oxygen exchange rates normalized per surface area of the catalyst (measured using N_2 physisorption). Oxygen exchange rates in each experiment were calculated on the basis of the variation of the $^{16}O^{18}O$ concentration as a function of time. Details are found in the Supporting Information.

Electrochemical Studies. Polarization resistances of the electrochemical oxygen exchange were measured using symmetric electrochemical cells. The symmetric cells were characterized by a relatively thick electrolyte (~360 μm) and two identical electrodes. The electrolyte was prepared by pressing YSZ powder into 13-mm-diameter pellets, followed by sintering at 1723 K for 4 h. A porous 8 mol% yttria stabilized zirconia (YSZ) scaffold layer for the electrode was synthesized to support the LNO nanostructured electrocatalysts. The presynthesized LNO catalyst was dispersed in ethanol and sequentially impregnated on the YSZ scaffold, followed by heating at 673 K for 3 h. A similar approach was used to synthesize anode-supported SOFCs. For all SOFCs, the anode was kept constant at a composition of 50 wt % of Ni oxide and 50 wt % of YSZ. Similarly, the YSZ electrolyte layer was kept constant by spin-coating a given amount of YSZ slurry over the anode pellet. Details are found in the Supporting Information.

Electrochemical impedance spectroscopy (EIS) was performed on the symmetric cells using a potentiostat (Gamry 300, Gamry Inst. Warminster, PA). EIS data were obtained at open circuit voltage (OCV) in a frequency range of 1 MHz−0.01 Hz with 10 mV of AC perturbation.[15] The experiments were performed in a single chamber reactor under a controlled O_2/N_2 atmosphere (with oxygen partial pressure, p_{O_2}, between 0.04 and 1 atm). Details on the electrochemical studies using SOFCs are found in the Supporting Information.

RESULTS AND DISCUSSION

DFT Calculations of Oxygen Exchange on LNO Surfaces. To identify the underlying factors that govern the oxygen exchange kinetics on nickelate oxides and potentially obtain insight on optimizing their surface reactivity toward the oxygen reduction reaction, we have employed DFT calculations to determine the energetics associated with the thermochemical oxygen exchange process on nickelate oxides, through the example of LNO with different surface facets.

The four most thermodynamically stable surfaces are considered: namely, (001)-Ni oxide-terminated, (001)-La oxide-terminated, and (100) and (111) LNO surfaces.[6c] The surface oxygen-exchange process on LNO was modeled using two reversible elementary steps (illustrated in Figure 1b):[6d,e] (i) the formation of surface oxygen vacancies via migration of oxygen ions to the surface bulk interstitial oxygen sites known as the Frenkel disorder (the most favorable path for oxygen transport in nickelates)[16] and (ii) oxygen dissociative adsorption on a surface oxygen vacant site to heal the vacancy and form an oxygen adatom. The reverse reactions of these two steps occur to complete the catalytic cycle. Assuming similar charge transfer coefficients of elementary steps for different surfaces, the kinetics obtained for the oxygen exchange without external potentials can provide valuable insights into the electrochemical processes.

Figure 1c shows the free energy surfaces for the thermochemical surface oxygen exchange process. We found that the surface vacancy formation is highly endothermic by 3.19 and 3.34 eV on (001)-La oxide-terminated and (100) surfaces, respectively; however, on (001)-Ni oxide-terminated and (111) surfaces, the surface oxygen vacancy formation becomes facile, with free energy barriers of 0.48 and 0.71 eV, respectively. The dissociation of O_2 on the surface vacant sites formed on a (001)-La oxide-terminated surface is almost barrierless as a result of the significantly stronger binding energies for oxygen on the vacant site and the oxygen adatom on the La bridge site (Table S1 and Figure S2 of the Supporting Information). Consequently, this results in a very high barrier (6.75 eV) for the reverse step, which hinders the exchange process. A similar trend is obtained for the (100) LNO surface, where the barrier for the association of O_2 (step 2, reverse) is 6.61 eV and for O_2 dissociation is 0.76 eV. In the case of (001)-Ni oxide-terminated LNO surface, a compromise between the energies for these steps is obtained. The dissociation of O_2 is limiting and is slightly endergonic by 0.15 eV, with a kinetic barrier of 1.73 eV. This is also the case for the (111) LNO surface, but the dissociation barrier of O_2 is 0.35 eV higher than that of the (001)-Ni oxide terminated LNO surface.

From the energetics of the reaction pathway, we found that the rate-limiting step for the surface oxygen exchange on (001)-La oxide-terminated and (100) surfaces is the associative oxygen desorption (step 2, reverse). On the other hand, the rate-limiting step on (111) and (001)-Ni oxide-terminated surfaces is the dissociative adsorption (step 2, forward) of O_2. Moreover, the barriers for the rate-limiting step on (001)-La oxide-terminated (6.75 eV), (100) (6.61 eV), and (111) (2.08 eV) surfaces are higher than that on the (001)-Ni oxide-terminated surface (1.73 eV). These results suggest that the

DOI: 10.1021/acscatal.5b00756
ACS Catal. 2015, 5, 4013−4019

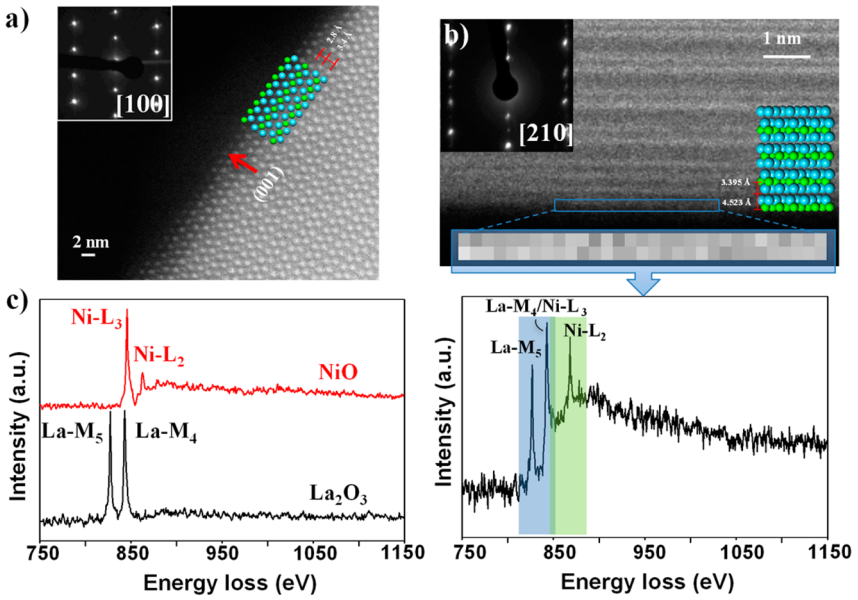

Figure 2. (a) Atomic-resolution HAADF image taken from a typical LNO nanorod with the electron beam parallel to [100] (i.e., parallel to the (001) plane). The upper-right inset illustrates a [001] projected DFT model structure along the [100] direction with La (light blue) and Ni (green) atoms labeled, along with the lattice spacing (the oxygen atoms have been removed from the DFT model to ease the eye). (b) HAADF image taken from another nanorod along the [210] direction (as evidenced by the SAED inset) with the (001) plane labeled. The surface layer (0.3 nm deep) is outlined by the blue box from which a summed EELS spectrum was extracted from an EELS spectrum imaging data set at 0.15 nm pixel size showing the partly overlapped Ni ($L_{2,3}$) and La ($M_{4,5}$) edges. (c) Standard EELS spectra for NiO and La_2O_3.

(001)-Ni oxide-terminated LNO surfaces should exhibit the highest rates for surface oxygen exchange as compared with the other LNO surfaces. This is confirmed using a simple microkinetic modeling analysis (Supporting Information).

The calculated rates for the thermochemical surface oxygen exchange at an operating temperature of 773 K and 0.21 atm partial pressure of O_2 on these four surfaces are shown in Figure 1d. The predicted trend of thermochemical oxygen exchange activity is a consequence of (100) and (001)-La oxide-terminated surfaces' very strong binding of the lattice oxygen, resulting in a high-energy barrier for oxygen recombination to form gas-phase O_2. On the other hand, the (001)-Ni oxide-terminated LNO surface facilitates the best compromise between the energetics associated with surface oxygen vacancy formation and the oxygen adsorption/desorption steps, which results in the highest rate. On the basis of these findings, one would predict that synthesizing LNO catalysts with a high concentration of (001)-Ni oxide-terminated surface facets would lead to LNO catalysts with improved oxygen exchange kinetics as compared with traditional LNO catalysts.

Synthesis of Well-Controlled LNO Nanostructures. Recently, we demonstrated the ability to synthesize LNO nanostructures with well-defined surface facets using a reverse microemulsion approach.[13] The method involved (i) the formation of a gel containing the appropriate metal hydroxide precursors, (ii) separation of the solid gel from reaction mixture, and (iii) transformation of the precursors to nickelate oxides by calcination. Tuning the synthesis parameters led to nanostructured LNO catalysts with two different geometries: polyhedrons (spheres, similar to the geometry of traditional catalysts) and nanorods (Figure S3a,b; c,d, respectively of the Supporting Information). The LNO nanorods were highly terminated by (001) facets, as described in detail in our previous report,[13] and also shown by the selective area electron diffraction (SAED) pattern (Figure S 3d, Supporting Information). On the other hand, the LNO spheres were terminated by a mixture of different surface planes, including the (111) facet, as indicated by the SAED pattern (Figure S3b, Supporting Information) of a typical spherical particle.[13]

Above, our DFT calculations suggested that the (001) surface of LNO is either Ni oxide- or La oxide-terminated, with the Ni oxide-terminated surface being the most active. To characterize the atomic termination of the (001) surface facets of the LNO nanorods, we have employed atomic resolution HAADF and EELS performed in an aberration-corrected STEM. Figure 2a shows an atomic resolution HAADF image of the edge of a typical LNO nanorod with the electron beam along the [100] zone axis (i.e., parallel to the (001) plane), as indicated by the SAED pattern (upper left inset in Figure 2a). The upper right inset in Figure 2a shows the projected DFT model structure ((001)-Ni oxide-terminated) that best matches the lattice spacing and the atom species in the HAADF image (note that the DFT model does not show the oxygen atoms because they are not visible in the HAADF image). Figure 2a shows that the surface termination of the LNO nanorod supports the (001)-Ni oxide terminated LNO model structure, suggesting that the surface is terminated by Ni oxide. The arrangements of the La atoms in the surface layers are not consistent with the reported (001) La oxide-terminated surface (shown in Figure S1, Supporting Information).[5b] This is further supported by atomic resolution EELS spectrum imaging analysis (at a pixel size of 0.15 nm), which is used to map out the (001) chemistry, as shown in Figure 2b. Figure 2b shows the HAADF image taken from another LNO nanorod with the electron beam parallel to [210] (parallel to (001) plane), and the summed EELS spectrum showing the Ni-$L_{2,3}$ and La-$M_{4,5}$ edges of the surface region.

A Ni/La atomic ratio of ~3.7 was obtained by MLLS fitting of the spectrum using the EELS spectra taken from commercial

DOI: 10.1021/acscatal.5b00756
ACS Catal. 2015, 5, 4013−4019

La_2O_3 and Ni oxide samples (Figure 2c) under the same experimental conditions as references. Because the (001) surface contains only Ni or La atoms, we believe that the La signal is most likely due to the La atoms present in the second atomic layer. These surface characterization studies suggest that the (001) surfaces of the LNO nanorods are terminated by Ni oxide and, on the basis of the DFT predictions, should result in the highest activity for oxygen exchange.

Oxygen Exchange Kinetics. The kinetics of the thermochemical oxygen surface exchange over LNO catalysts with different geometries (i.e., spheres, nanorods) were studied using steady state isotopic transient kinetic analysis in a flow reactor. The experiments were conducted in a temperature range of 723−923 K. In these studies, the catalyst was first saturated with $^{16}O_2$ and then exposed to $^{18}O_2$ to determine the rates of oxygen exchange between ^{18}O in the gas phase and ^{16}O in the lattice of LNO. The rate of oxygen exchange was defined as the formation rate of $^{16}O^{18}O$ over time, as measured by a mass spectrometer system online with the reactor. The apparent activation barrier for this process was determined by measuring the initial rates of $^{16}O^{18}O$ formation at different temperatures. The absence of mass transport artifacts was verified to ensure that the rates reflect the intrinsic oxygen surface exchange kinetics (see Supporting Information for details). Arrhenius plots of the oxygen exchange rates (normalized per surface area, labeled as turnover frequencies (TOFs)) over LNO nanorods and spheres are shown in Figure 3. The apparent activation energy barrier for the oxygen

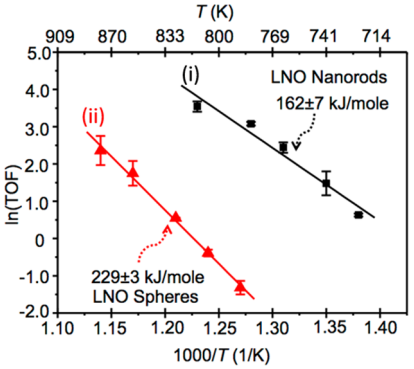

Figure 3. Apparent activation barriers obtained from thermochemical oxygen exchange kinetics, LNO spheres and nanorods. The error bars represent the standard deviation obtained from three consecutive experiments.

exchange (extracted from the slope of the Arrhenius plot) catalyzed by LNO nanorods is much lower than that for LNO with spherical geometry. This is consistent with the DFT trends, which show that the (001)-Ni oxide-terminated LNO surface (abundant in the synthesized LNO nanorods) exhibits the lowest energy barrier for oxygen exchange as compared with the other low-energy facets (i.e., (111)) that are found in spherical LNO particles. Post reaction characterization of the catalysts using XRD and SEM (Figures S6, S7 and S8, Supporting Information) shows that both the nanorod- and spherical-shaped LNO catalysts were stable and retained their structures after the oxygen exchange kinetic studies.

Electrochemical Oxygen Exchange and Oxygen Reduction. Polarization resistances of the electrochemical oxygen exchange on electrodes containing LNO catalysts with different geometries were measured using symmetric LNO|YSZ|LNO cells with yttria-stabilized zirconia (YSZ) as an oxygen ion conducting membrane. The details of the synthesis of the symmetric cells are provided in the Theoretical and Experimental section. The impedance studies were conducted at 873 and 973 K under various O_2 partial atmospheres. An equivalent circuit of the type $LR_e(R_1Q_1)(R_2Q_2)$ (Figure 4a) was fitted to the raw EIS data. In this model, L represents the inductance caused by the electrical connections, R_e represents the ohmic resistance of the YSZ electrolyte, and the circuit elements composed of a resistance in parallel with a constant phase element (R_1Q_1 and R_2Q_2) represent the cathodic resistances at high (HF) and low frequency (LH) ranges, respectively. The area-specific resistance (ASR) which accounts for oxygen exchange at both interfaces was obtained from the raw data using the following expression: $ASR = (R_1 + R_2) \times S/2$, where S is the electrode active area (accounts for the surface area of the catalyst).[17]

Figure 4a shows the ASR of symmetric cells containing LNO nanorods (LNO-nanorods|YSZ|LNO-nanorods) and LNO spheres (LNO-spheres|YSZ|LNO-spheres) at different oxygen partial pressures (p_{O_2}). In these plots, the R_e values were normalized to the lowest value, and the inductance was removed for ease of illustration of the R_1 and R_2 dependence on p_{O_2} (the raw data with aspect ratio 1:1 is found in Figure S9 of the Supporting Information). Linear dependences between the two resistances (R_1 and R_2) and p_{O_2} with slopes around 0.1 and 0.2, respectively, for cells containing nanorods and spheres were obtained. This is consistent with literature reports that suggest that this behavior is associated with the fact that R_1 and R_2 are related to the process of oxygen ion transfer through the electrode/electrolyte interface ($O_{ads} + 2e^- + V_O^{\bullet\bullet} \Leftrightarrow O_O^X$), and the vacancy healing/charge transfer step through the gas/electrode interface ($O^{2-} + V_O^{\bullet\bullet} \Leftrightarrow O_O^X$), respectively.[18] Furthermore, the capacitances (C_1 and C_2) for R_1 and R_2 in both cells containing rods and spheres were around 10^{-6} and 10^{-4} F*cm^{-2}, respectively, reinforcing the fact that these impedance behaviors are related to the oxygen exchange process (Figure S10, Supporting Information).[19]

ASRs for symmetric cells composed of LNO nanorods and LNO spheres at two different temperatures (similar to the operating temperatures of a fuel cell) are plotted in Figure 4b. These results show that the ASRs for LNO nanorod-containing cells are significantly lower than the ones for the cells containing the LNO spheres at both temperatures. Analysis of these impedance spectra demonstrates that the LNO-nanorods|YSZ|LNO-nanorods cells exhibit lower overpotential losses for the electrochemical surface oxygen-exchange process, which includes the oxygen ion transfer to the electrolyte (R_1) and vacancy healing/charge transfer (R_2) steps.

To test the electrochemical performance toward oxygen reduction in fuel cells, the LNO nanostructures were incorporated in anode-supported SOFCs (Ni-YSZ|YSZ|YSZ-LNO). In SOFCs, the anode facilitates the hydrogen electro-oxidation reaction ($H_2 + O^{2-} \Rightarrow H_2O + 2e^-$), the YSZ electrolyte (~15 μm) facilitates the oxygen ion (O^{2-}) transport, and the cathode facilitates the oxygen reduction reaction ($^1/_2\ O^2 + 2e^- \Rightarrow O^{2-}$). Figure 4c shows the electrochemical performance (current density versus voltage (I−V) and current density versus power density (I−P) curves) of SOFCs operating on pure H_2 at the anode and air at the cathode at a temperature of 973 K. The results show that upon modification of the LNO nanostructure from rods to spheres,

DOI: 10.1021/acscatal.5b00756
ACS Catal. 2015, 5, 4013−4019

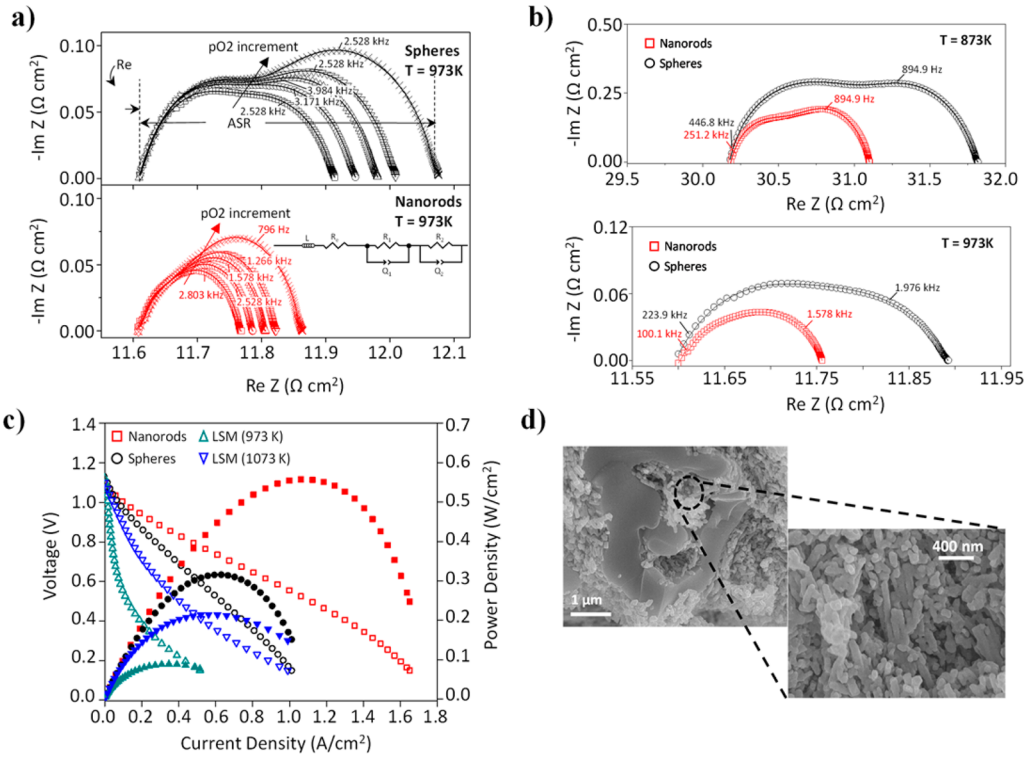

Figure 4. (a) EIS at the OCV for LNO-nanorods|YSZ|LNO-nanorods (red) and LNO-spheres|YSZ|LNO-spheres cells (black) at different partial pressures: 0.8 atm (□), 0.4 atm (○), 0.21 atm (Δ), 0.13 atm (∇), and 0.04 atm (X). (b) Cathodic polarization dependence of LNO-nanorods|YSZ|LNO-nanorods and LNO-spheres|YSZ|LNO-spheres cells on temperature. (c) Current density versus voltage, and current density versus power density curves for SOFCs containing LNO cathode electrocatalysts with different morphologies: nanorods and spheres, operating at 973 K, and SOFCs with cathodes containing LSM operating at 973 and 1073 K. All cells were tested with the anode exposed to pure H_2 and the cathode exposed to air. (d) Scanning electron micrographs of a SOFC cathode containing LNO nanorod electrocatalyst after the electrochemical studies.

significant improvement in the power density was achieved. SOFCs containing LNO nanorods as the cathode electrocatalyst led to power densities ~2-fold higher than the cells containing LNO spheres as the cathode electrocatalyst: ~ 0.6 and 0.3 W/cm^2, respectively. Furthermore, we found that the performance of the SOFC composed of Ni-YSZ|YSZ|YSZ-LNO-nanorods at 973 K was also superior to SOFCs containing state-of-the-art lanthanum strontium manganite (LSM) cathode electrocatalyst (Ni-YSZ|YSZ|YSZ-LSM) at operating temperatures of 973 and 1073 K (Figure 4c).

SEM characterization of the cells after the electrochemical tests shows no significant changes in the morphology (Figure 4d and Figure S11, Supporting Information) of the LNO nanostructures. The stability of the LNO nanorods was also tested by operating the SOFC under constant current (700 mA/cm^2) while monitoring the voltage over 70 h at 973 K (Figure S12 a, Supporting Information). No significant changes in the morphology (Figure S12 b, Supporting Information) and crystallinity (Figure S13, Supporting Information) of LNO nanorods were observed after the constant-current electrochemical test. These results suggest that the LNO nanorod catalysts, while retaining their structural and morphological stability, exhibit superior electrochemical activity toward the oxygen reduction reaction as compared with the traditional, state-of-the-art catalysts. These results demonstrate the impact of utilizing well-defined nanostructures of mixed ionic and electronic conducting oxide electrocatalyst in enhancing the oxygen reduction kinetics in ceramic-based fuel cells.

CONCLUSIONS

We have established that the surface structure of complex oxides (e.g., LNO) plays an important role in their catalytic activity toward oxygen exchange/reduction, with the (001)-Ni oxide-terminated surface being the most active. Isotopic exchange kinetic experiments and electrochemical studies show that LNO catalysts with nanorod geometry (highly populated by (001)-Ni oxide-terminated facets) exhibit higher rates for oxygen exchange and reduction as compared with traditional spherical LNO catalysts. DFT studies suggest that the enhanced activity of LNO nanorods is attributed to the high fraction of (001)-Ni oxide-terminated surface facets, which provide the best compromise of the energetics associated with two important steps in oxygen exchange/reduction: surface oxygen vacancies and dissociative adsorption of gas phase O_2. These findings have significant implications in guiding the design of robust mixed ionic and electronic catalysts for processes involving oxygen based on controlling their nanostructure.

ASSOCIATED CONTENT

Supporting Information

The Supporting Information is available free of charge on the ACS Publications website at DOI: 10.1021/acscatal.5b00756.

Details of computational methodology, synthesis methods, characterization, kinetic isotope reaction, fabrication of solid oxide fuel cell, and electrochemical studies (PDF)

DOI: 10.1021/acscatal.5b00756
ACS Catal. 2015, 5, 4013−4019

AUTHOR INFORMATION

Corresponding Author

*E-mail: erandan@wayne.edu.

Author Contributions

⊥X.M., J.S.A.C., and X.-K.G. contributed equally.

Notes

The authors declare no competing financial interests.

ACKNOWLEDGMENTS

We thank the financial support from Wayne State University and WSU Office of Vice President for Research. The JEOL JEM-3100R05 double aberration-corrected microscope was sponsored by NSF through the grant #DMR-0723032 operated at the Electron Microbeam Analysis Laboratory at the University of Michigan. We would like to acknowledge the support from the Extreme Science and Engineering Discovery Environment (XSEDE) for computational resources and Prof. Jeff Greeley for assistance with the computational work.

REFERENCES

(1) (a) Xie, X. W.; Li, Y.; Liu, Z. Q.; Haruta, M.; Shen, W. J. *Nature* **2009**, *458* (7239), 746−749. (b) Behrens, M.; Studt, F.; Kasatkin, I.; Kuhl, S.; Havecker, M.; Abild-Pedersen, F.; Zander, S.; Girgsdies, F.; Kurr, P.; Kniep, B. L.; Tovar, M.; Fischer, R. W.; Norskov, J. K.; Schlogl, R. *Science* **2012**, *336* (6083), 893−897. (c) Tian, N.; Zhou, Z. Y.; Sun, S. G.; Ding, Y.; Wang, Z. L. *Science* **2007**, *316* (5825), 732−735. (d) Christopher, P.; Linic, S. *J. Am. Chem. Soc.* **2008**, *130* (34), 11264−11265. (e) Sanchez-Sanchez, C. M.; Solla-Gullon, J.; Vidal-Iglesias, F. J.; Aldaz, A.; Montiel, V.; Herrero, E. *J. Am. Chem. Soc.* **2010**, *132* (16), 5622−5624. (f) Hua, Q.; Cao, T.; Gu, X. K.; Lu, J. Q.; Jiang, Z. Q.; Pan, X. R.; Luo, L. F.; Li, W. X.; Huang, W. X. *Angew. Chem., Int. Ed.* **2014**, *53* (19), 4856−4861.

(2) (a) Linic, S.; Christopher, P. *ChemCatChem* **2010**, *2* (9), 1061−1063. (b) Christopher, P.; Linic, S. Shape- and Size-Specific Chemistry of Ag Nanostructures in Catalytic Ethylene Epoxidation. *ChemCatChem* **2010**, *2* (1), 78−83.

(3) (a) Sayers, R.; Rieu, M.; Lenormand, P.; Ansart, F.; Kilner, J. A.; Skinner, S. J. *Solid State Ionics* **2011**, *192* (1), 531−534. (b) Chauveau, F.; Mougin, J.; Mauvy, F.; Bassat, J. M.; Grenier, J. C. *Int. J. Hydrogen Energy* **2011**, *36* (13), 7785−7790. (c) Jung, K. N.; Jung, J. H.; Im, W. B.; Yoon, S.; Shin, K. H.; Lee, J. W. *ACS Appl. Mater. Interfaces* **2013**, *5* (20), 9902−9907. (d) Read, M. S. D.; Islam, M. S.; King, F.; Hancock, F. E. *J. Phys. Chem. B* **1999**, *103* (9), 1558−1562.

(4) Bassat, J. M.; Odier, P.; Villesuzanne, A.; Marin, C.; Pouchard, M. *Solid State Ionics* **2004**, *167* (3−4), 341−347.

(5) (a) Kan, C. C.; Kan, H. H.; Van Assche, F. M.; Armstrong, E. N.; Wachsman, E. D. *J. Electrochem. Soc.* **2008**, *155* (10), B985−B993. (b) Burriel, M.; Wilkins, S.; Hill, J. P.; Munoz-Marquez, M. A.; Brongersma, H. H.; Kilner, J. A.; Ryan, M. P.; Skinner, S. J. *Energy Environ. Sci.* **2014**, *7* (1), 311−316.

(6) (a) Kim, G.; Wang, S.; Jacobson, A. J.; Chen, C. L. *Solid State Ionics* **2006**, *177* (17−18), 1461−1467. (b) Shen, Y. N.; Zhao, H. L.; Liu, X. T.; Xu, N. S. *Phys. Chem. Chem. Phys.* **2010**, *12* (45), 15124−15131. (c) Read, M. S. D.; Islam, M. S.; Watson, G. W.; Hancock, F. E. *J. Mater. Chem.* **2001**, *11* (10), 2597−2602. (d) Kushima, A.; Parfitt, D.; Chroneos, A.; Yildiz, B.; Kilner, J. A.; Grimes, R. W. *Phys. Chem. Chem. Phys.* **2011**, *13* (6), 2242−2249. (e) Adler, S. B.; Chen, X. Y.; Wilson, J. R. *J. Catal.* **2007**, *245* (1), 91−109.

(7) (a) Kresse, G.; Furthmuller, J. *Phys. Rev. B: Condens. Matter Mater. Phys.* **1996**, *54* (16), 11169−11186. (b) Kresse, G.; Furthmuller, J. *Comput. Mater. Sci.* **1996**, *6* (1), 15−50.

(8) Perdew, J. P.; Burke, K.; Ernzerhof, M. *Phys. Rev. Lett.* **1996**, *77* (18), 3865−3868.

(9) Zhou, J.; Chen, G.; Wu, K.; Cheng, Y. H. *J. Phys. Chem. C* **2013**, *117* (25), 12991−12999.

(10) Dudarev, S. L.; Botton, G. A.; Savrasov, S. Y.; Humphreys, C. J.; Sutton, A. P. *Phys. Rev. B: Condens. Matter Mater. Phys.* **1998**, *57* (3), 1505−1509.

(11) Wang, L.; Maxisch, T.; Ceder, G. *Phys. Rev. B* **2006**, *73* (19), 10.1103/physrevb.73.195107.

(12) (a) Henkelman, G.; Uberuaga, B. P.; Jonsson, H. *J. Chem. Phys.* **2000**, *113* (22), 9901−9904. (b) Henkelman, G.; Jonsson, H. *J. Chem. Phys.* **2000**, *113* (22), 9978−9985.

(13) Ma, X.; Wang, B.; Xhafa, E.; Sun, K.; Nikolla, E. *Chem. Commun.* **2015**, *51* (1), 137−140.

(14) Gauquelin, N.; Benckiser, E.; Kinyanjui, M. K.; Wu, M.; Lu, Y.; Christiani, G.; Logvenov, G.; Habermeier, H. U.; Kaiser, U.; Keimer, B.; Botton, G. A. *Phys. Rev. B: Condens. Matter Mater. Phys.* **2014**, *90* (19), 195140.

(15) Lee, J. G.; Park, J. H.; Shul, Y. G. *Nat. Commun.* **2014**, *5*, 4045.

(16) Kittel, C. *Introduction to Solid State Physics*, 8th ed.; Wiley: Hoboken, NJ, 2005.

(17) Shao, Z. P.; Haile, S. M. *Nature* **2004**, *431* (7005), 170−173.

(18) Escudero, M. J.; Aguadero, A.; Alonso, J. A.; Daza, L. *J. Electroanal. Chem.* **2007**, *611* (1−2), 107−116.

(19) Philippeau, B.; Mauvy, F.; Mazataud, C.; Fourcade, S.; Grenier, J.-C. *Solid State Ionics* **2013**, *249*, 17−25.

DOI: 10.1021/acscatal.5b00756
ACS Catal. 2015, 5, 4013−4019